Supplementary Information

Metasurface-enabled Broadband Multidimensional Photodetectors

Hao Jiang[1], Yinzhu Chen[2,3], Wenyu Guo[1,4,5,6], Yan Zhang[1], Rigui Zhou[4,5], Mile Gu[1,6], Fan Zhong[3], Zhenhua Ni[3], Junpeng Lu[3,], Cheng-Wei Qiu[2,*] and Weibo Gao[1,*]*

[1]School of Physical and Mathematical Sciences, Nanyang Technological University, Singapore 639798, Singapore

[2]Department of Electrical and Computer Engineering, National University of Singapore, Singapore 117583, Singapore

[3]Key Laboratory of Quantum Materials and Devices of Ministry of Education, School of Physics, Southeast University, Nanjing 211189, China

[4]College of Information Engineering, Shanghai Maritime University, Shanghai 201306, China

[5]Research Center of Intelligent, Information Processing and Quantum Intelligent Computing, Shanghai 201306, China

[6] Centre for Quantum Technologies, National University of Singapore, Singapore

These authors contributed equally: Hao Jiang, Yinzhu Chen

[*] Email:

(J. P. L.) phyljp@seu.edu.cn

(C. W. Q.) chengwei.qiu@nus.edu.sg

(W. B. G.) wbgao@ntu.edu.sg

Supplementary Note 1

1. Device structure and characterization.

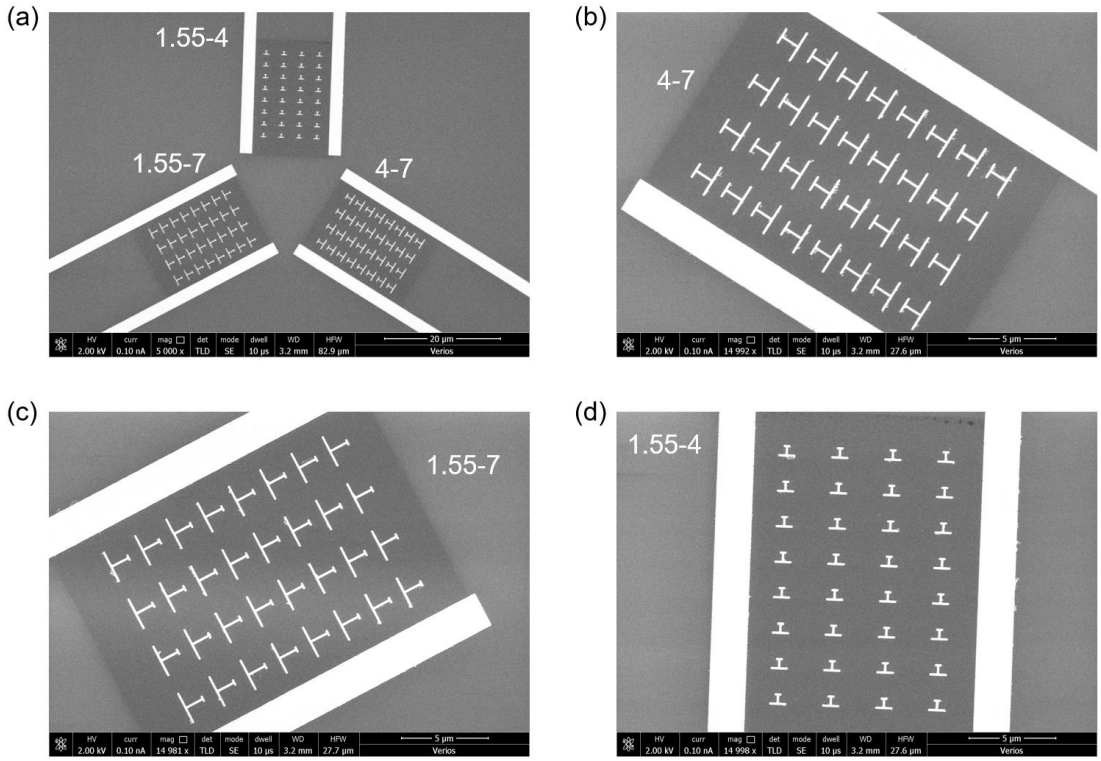

Supplementary Fig. 1 (a)-(d) SEM images of the overall three-port device and individual ports.

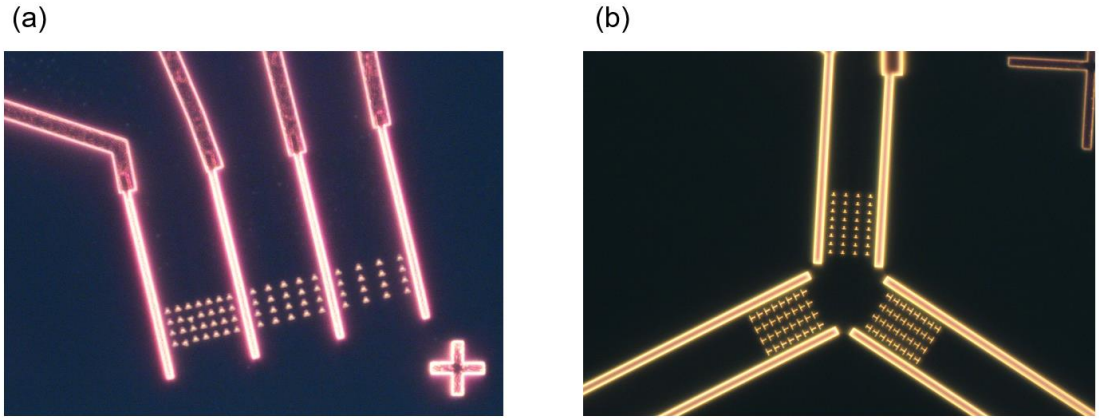

Supplementary Fig. 2. Microscopic dark-field images of the two-port (a) and three-port devices (b).

Supplementary Note 2

2. Near field mode and photocurrent analysis.

2.1. Analysis of near-field asymmetry using temporal coupled mode theory

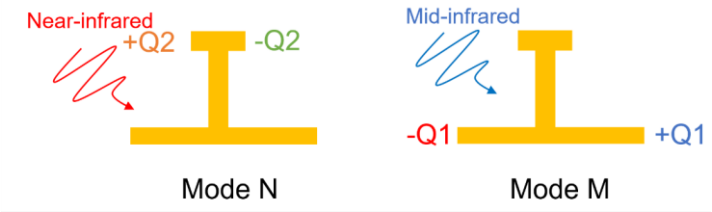

Supplementary Fig. 3. Two eigenmodes of the dual-arm plasmonic nanostructure under light with different wavelengths and circularly polarized states. +Q and −Q denote oscillating charges in plasmonic mode, with the "+" and "–" signs illustrating the relative phase to the incident light.

The mode interference of the plasmonic nanostructure under specifically polarized illumination can be described by the temporal coupled mode theory [1,2]:

$$\frac{d}{dt}\begin{pmatrix} n \\ m \end{pmatrix} = \begin{pmatrix} j\omega_n - \gamma_{ne} - \gamma_{ni} & \\ & j\omega_m - \gamma_{me} - \gamma_{mi} \end{pmatrix}\begin{pmatrix} n \\ m \end{pmatrix} + \begin{pmatrix} \kappa_n & \\ & \kappa_m \end{pmatrix}\begin{pmatrix} E_x \\ E_x \end{pmatrix} \quad \text{(S1)}$$

where n and m are the oscillation amplitudes of modes N and M, respectively, as shown in Supplementary Fig. 3. In addition, modes N and M have resonance frequencies (ω_n, ω_m), external decay rates (γ_{ne}, γ_{me}), internal decay rates (γ_{ni}, γ_{mi}), and coupling strengths to incident light (κ_n, κ_m), respectively. For dual-arm plasma nanostructures, modes N and M refer to two resonant modes observed under circularly polarized light at wavelengths of 1.55 μm (near-infrared) and 4 μm (mid-infrared), respectively. These modes are dominated by the short arm and long arm, respectively. E_x denotes the complex amplitude of the electric field of the light along the x-axis. Since both reflection and transmission are allowed in a single layer nanostructure array, the coupling strength is related to the external decay rates: $\kappa_a = \mathrm{sqrt}(\gamma_{ne})$; $\kappa_b = \mathrm{sqrt}(\gamma_{me})$.

The mode amplitude can be solved in the frequency domain by replacing d/dt with $j\omega$:

$$n = \frac{\kappa_n E}{j\omega - j\omega_n + \gamma_{ne} + \gamma_{ni}} \tag{S2}$$

$$m = \frac{\kappa_m E}{j\omega - j\omega_m + \gamma_{me} + \gamma_{mi}} \tag{S3}$$

The local field distribution can then be calculated after the mode profile and amplitude are known. The electric fields at the left edge, E_{L}, and right edge, E_{R}, of the nanostructure are

$$E_L \propto n - m = \frac{\kappa_n E}{j\omega - j\omega_n + \gamma_{ne} + \gamma_{ni}} - \frac{\kappa_m E}{j\omega - j\omega_m + \gamma_{me} + \gamma_{mi}} \tag{S4}$$

$$E_R \propto -n + m = -\frac{\kappa_n E}{j\omega - j\omega_n + \gamma_{ne} + \gamma_{ni}} + \frac{\kappa_m E}{j\omega - j\omega_m + \gamma_{me} + \gamma_{mi}} \tag{S5}$$

We then define the field asymmetry, also termed near-field chirality (*3*, *4*), as:

$$C = E_R^2 - E_L^2 \tag{S6}$$

which is a function of the resonance frequency, decay rate, and frequency of interest. Here, when the incident wavelength is 1.55 μm, m=0. Therefore, $E_L \propto n$ and $E_R \propto -n$ exhibit opposite electric field distributions for LCP and RCP light. When the incident wavelength is 4 μm, n=0. Therefore, $E_L \propto -\mathrm{m}$ and $E_R \propto m$. This is opposite to the near-field distribution of 1.55 μm circularly polarized incident light. Due to the different amplitudes of the mode indices m and n, circularly polarized light at wavelengths of 1.55 μm and 4 μm will result in electric field distributions with varying amplitudes and orientations.

2.2. Relationship between the near-field asymmetry and directional photoresponse

The role of the plasmonic nanostructure is twofold. First, it spatially modulates the optical field, leading to an inhomogeneous field profile: $\boldsymbol{E}(x, y)$. Second, the metallic nanostructures spatially modulate the doping level of the graphene sheet [5,6] and hence the Seebeck coefficient, $S(x, y)$ [7]. Upon optical illumination, a local photoresponse will be established through the photothermoelectric effect, $\boldsymbol{J}(x, y) \propto |\boldsymbol{E}|^2(x, y)\cdot\nabla S(x, y)$. After that, the transport of the local photoresponse is affected by many factors, such as the inhomogeneous conductance of the device channel. As a result, the calculation of the overall photoresponse, $\boldsymbol{J}_{\text{tot}}$, is complicated and only possible through numerical modeling. However, we can write the analytic expression of $\boldsymbol{J}_{\text{tot}}$ by defining a vectorial local responsivity, $\boldsymbol{\sigma}(x, y)$, as:

$$\vec{J}_{tot} = \iint_{x,y} \left|\vec{E}(x,y)\right|^2 \cdot \vec{\sigma}(x,y)dxdy \tag{S7}$$

Without loss of generality, we can assume a rectangular range of integrals, $x \in (-x_0, x_0)$ and $y \in (-y_0, y_0)$.

Since our plasmonic nanostructure is achiral, $\boldsymbol{\sigma}(x, y)$ should be parity-odd regarding the reflection operation, $x \rightarrow -x$, meaning that $\boldsymbol{\sigma}(-x, y) = -\boldsymbol{\sigma}(x, y)$. The equation of $\boldsymbol{J}_{\text{tot}}$ can then be rewritten:

$$\vec{J}_{tot} = \iint_{x,y} \left(\left|\vec{E}(x,y)\right|^2 - \left|\vec{E}(-x,y)\right|^2 \right) \cdot \vec{\sigma}(x,y)dxdy \tag{S8}$$

In the above equation, the range of the integral is halved, $x \in (0, x_0)$ and $y \in (-y_0, y_0)$. Note that the term $|\boldsymbol{E}|^2(x, y) - |\boldsymbol{E}|^2(-x, y)$ is indeed the near-field asymmetry defined in Eq. S6. Therefore, the CPL-sensitive vectorial photoresponse scales with the near-field asymmetry.

2.3. Numerical simulation of the photocurrent

To simulate the global photoresponse in such a strongly correlated system, we should consider the collective behavior of carriers in graphene and hence use hydrodynamic equations for modeling: [8,9]

$$\frac{\partial u(\mathrm{r})}{\partial t} = -\gamma u(\mathrm{r}) - (u(\mathrm{r})\cdot\nabla)u(\mathrm{r}) + \nu\nabla^2 u(\mathrm{r}) - \frac{1}{\rho}\nabla\phi(\mathrm{r}) + F(\mathrm{r}) \qquad \text{(S9)}$$

where $\boldsymbol{u}(\mathrm{r})$ is the velocity of the charge carriers and $\phi(\mathrm{r})$ is the electric potential in the 2D plane. γ represents the ohmic damping factor. ν and ρ are the viscosity and density of electrons in graphene, respectively. $F(\mathrm{r})$ denotes the spatially distributed source term assumed to scale with the local photoresponse at the metal-graphene interfaces. At equilibrium where $\partial/\partial\mathrm{t} = 0$, the driving force is balanced by the ohmic damping of electrons or the friction of the nonslip boundaries of devices. For a given charge density in graphene, n, we can further derive the current density, $\boldsymbol{J}(\mathrm{r}) = \boldsymbol{u}(\mathrm{r})\cdot\mathrm{n}$. In a two-dimensional structure such as our device, the vectors only possess two components, so Equation S9 can be rewritten as:

$$\frac{\partial u_x}{\partial t} = -\gamma u_x - u_x\frac{\partial u_x}{\partial x} - u_y\frac{\partial u_y}{\partial y} + \nu\left(\frac{\partial^2 u_x}{\partial x^2} + \frac{\partial^2 u_y}{\partial y^2}\right) - \frac{1}{\rho}\frac{\partial\phi}{\partial x} + F_x \qquad \text{(S10)}$$

and

$$\frac{\partial u_y}{\partial t} = -\gamma u_y - u_y\frac{\partial u_y}{\partial x} - u_y\frac{\partial u_y}{\partial y} + \nu\left(\frac{\partial^2 u_y}{\partial x^2} + \frac{\partial^2 u_y}{\partial y^2}\right) - \frac{1}{\rho}\frac{\partial\phi}{\partial y} + F_y \qquad \text{(S11)}$$

The electric potential, Φ, can be recovered from the current distribution as [147]:

$$-\left(\frac{1}{\rho}\frac{\partial^2\phi}{\partial x^2} + \frac{1}{\rho}\frac{\partial^2\phi}{\partial y^2}\right) = \frac{\partial u_x}{\partial x}\frac{\partial u_x}{\partial x} + 2\frac{\partial u_x}{\partial y}\frac{\partial u_y}{\partial x} + \frac{\partial u_y}{\partial y}\frac{\partial u_y}{\partial y} \qquad \text{(S12)}$$

In our device with no external electrical bias, the source term originates from the local photocurrents, which are assumed to scale with the electrical field intensity, $|\mathrm{E}|^2$, and the gradient of the Seebeck coefficient, S:

$$F_x \propto \frac{\partial S}{\partial x}\cdot|E|^2 \qquad \text{(S13)}$$

and

$$F_y \propto \frac{\partial S}{\partial y}\cdot|E|^2 \qquad \text{(S14)}$$

Equations S9-S13 allow us to simulate the nanoantenna-driven current flow in graphene. The current distributions of the device under illumination with circularly polarized light

(LCP and RCP) at different wavelengths (1.55 μm and 4 μm) can be calculated, and the results are depicted in Supplementary Fig.4-7.

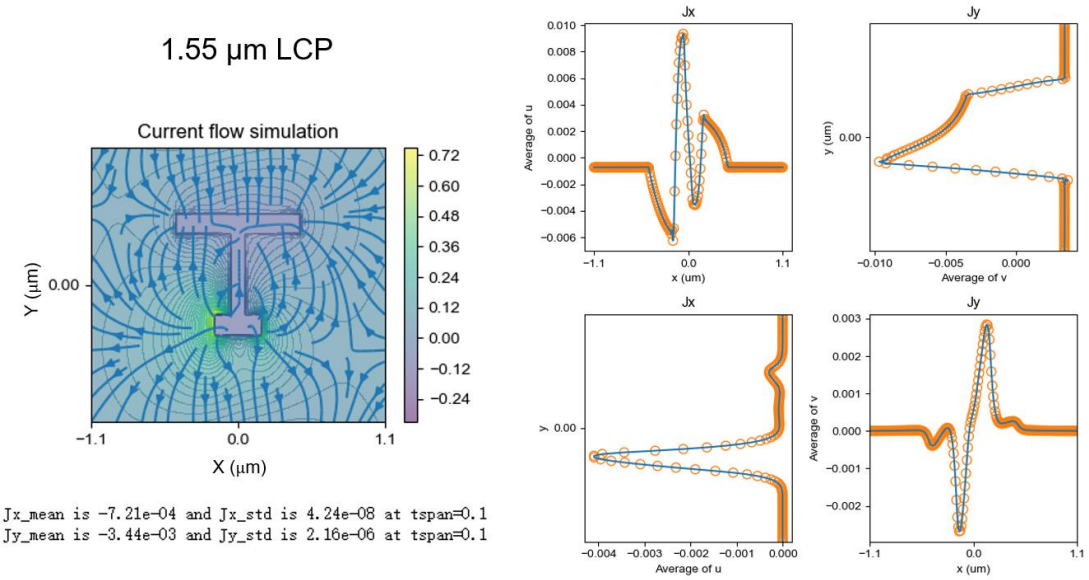

Supplementary Fig. 4. The simulated global current flow of dual-arm plasmonic nanostructures under LCP illumination at a wavelength of 1.55 μm.

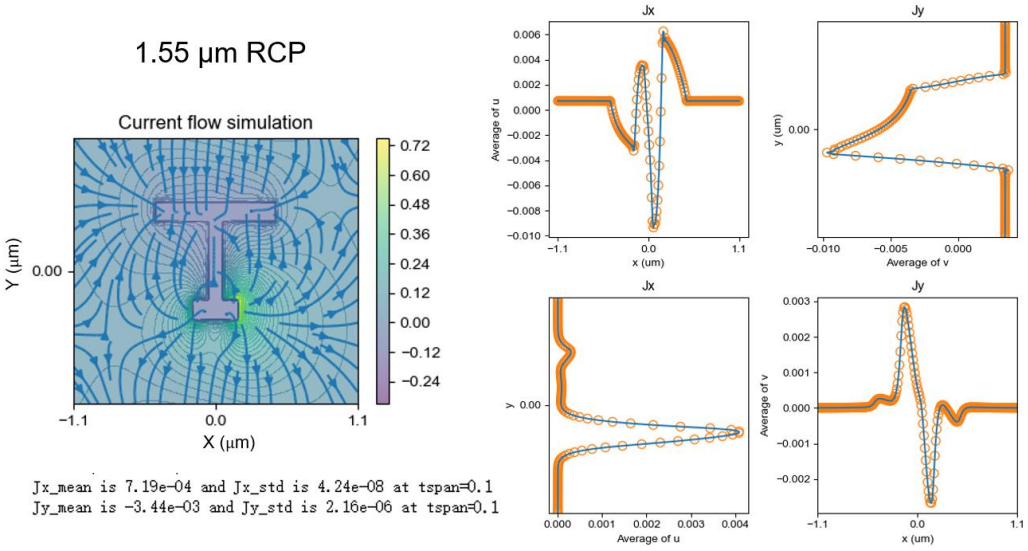

Supplementary Fig. 5. The simulated global current flow of dual-arm plasmonic nanostructures under RCP illumination at a wavelength of 1.55 μm.

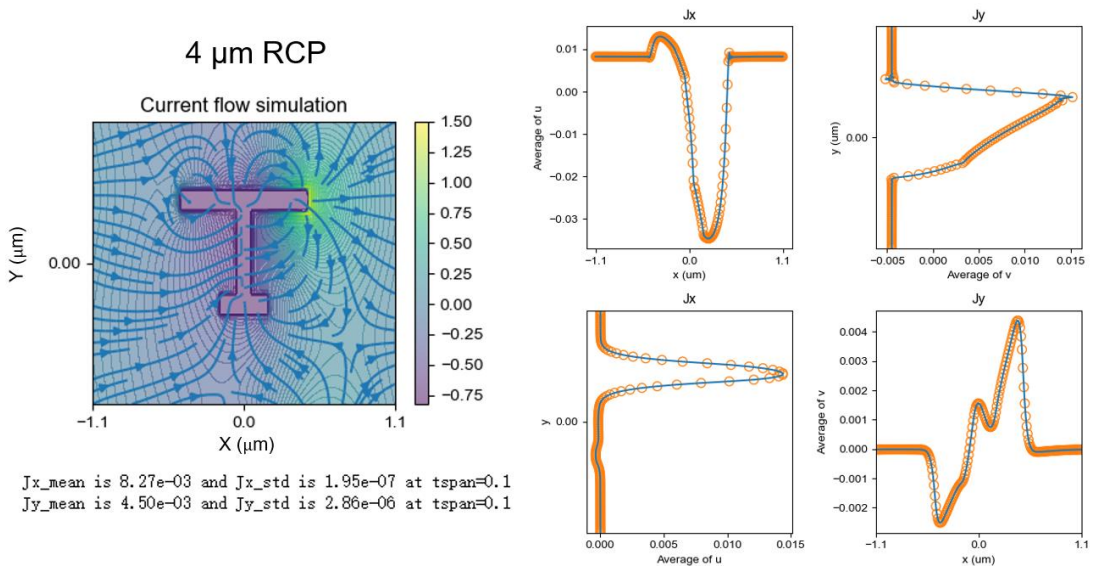

Supplementary Fig. 6 The simulated global current flow of dual-arm plasmonic nanostructures under RCP illumination at a wavelength of 4 μm.

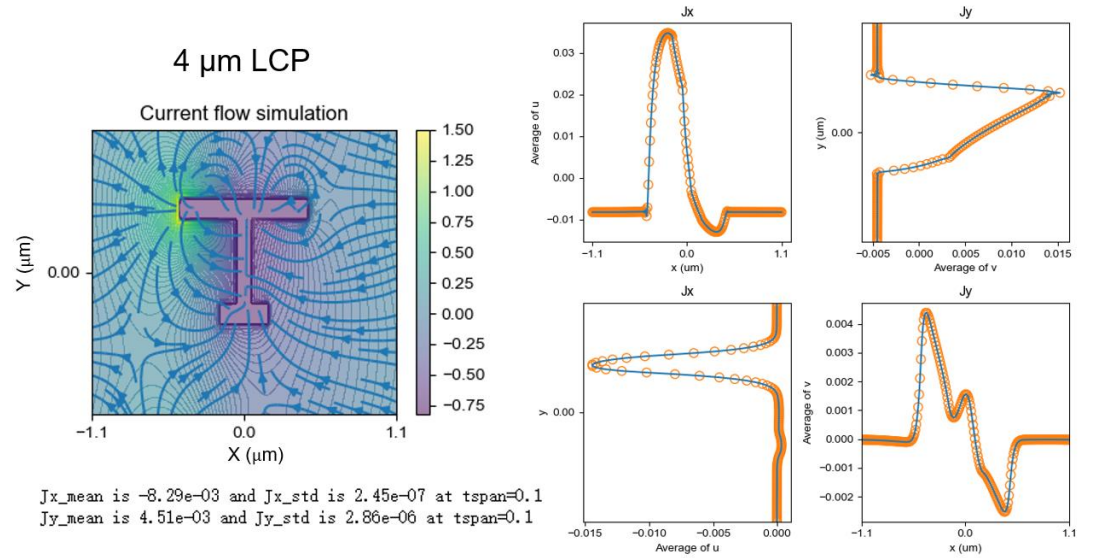

Supplementary Fig. 7. The simulated global current flow of dual-arm plasmonic nanostructures under LCP illumination at a wavelength of 4 μm.

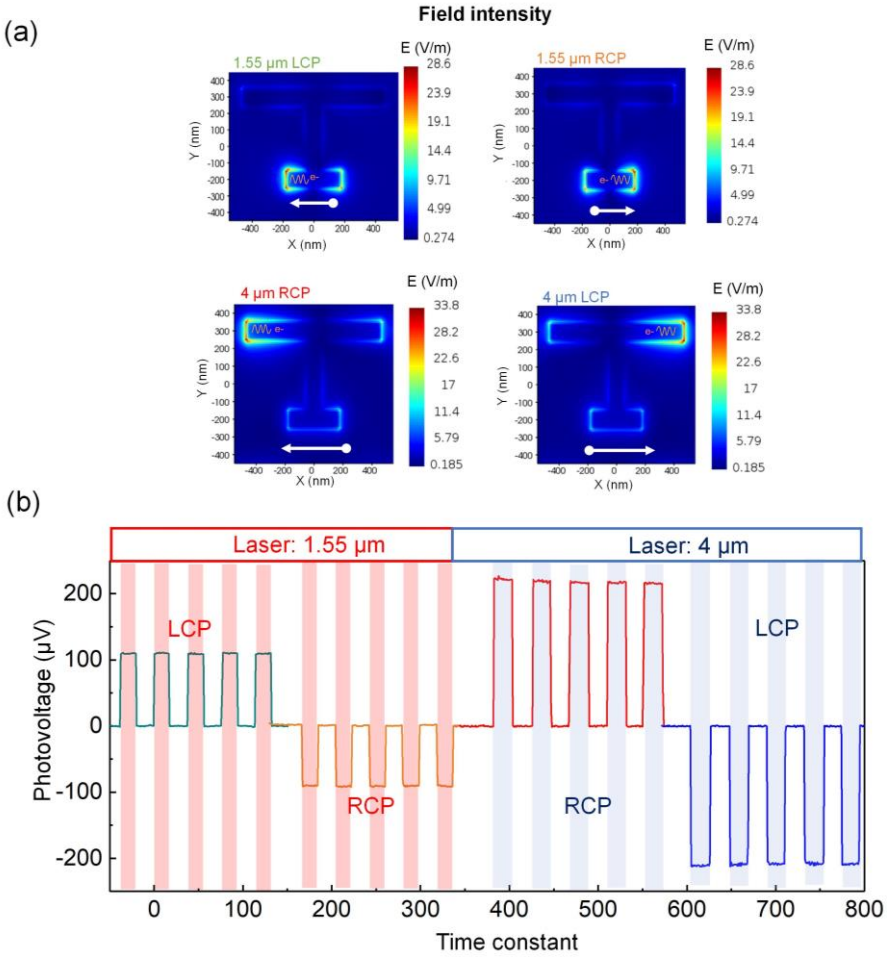

Supplementary Fig. 8. (a) Simulated near-field distribution in a unit cell at different wavelengths and circular polarization states of incident light. Yellow arrows indicate the flow of photocarriers generated at the nanoantenna–graphene interfaces. The white arrows illustrate the resultant vectorial photocurrents. (b) The photovoltage and photocurrent switching signal of the device under irradiation with 1.55 μm and 4 μm lasers at different circular polarizations.

The calculated photocurrent patterns resulting from the formed plasmonic nanostructures are highly consistent with the experimental measurements, as shown in Supplementary Fig. 8. For the two wavelengths (1.55 μm and 4 μm), the device exhibits a photovoltage of equal magnitude and opposite polarity under LCP and RCP illumination. Furthermore, for light of the same circular polarization state, the device generates photovoltages of unequal magnitude and opposite polarity under illumination with different wavelengths. This structural design significantly discriminates between different circular polarization states at two different wavelengths. This alignment suggests that the model can effectively predict experimental phenomena in a reasonable manner.

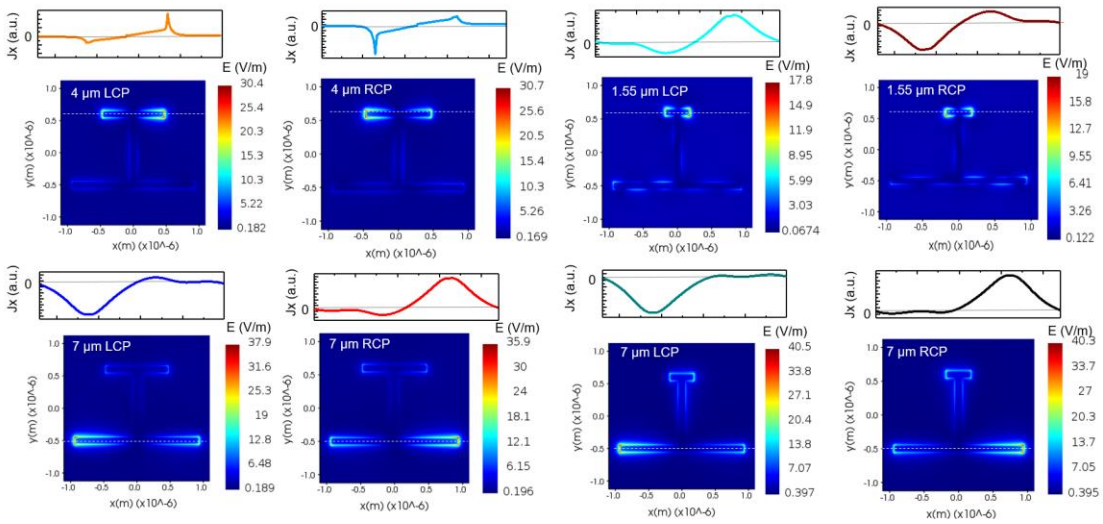

Supplementary Fig. 9. The near-field distribution and local photocurrent patterns of the plasmonic nanostructures in the 4-7 port device and the 1.55-7 port device.

Adjusting the lengths of the dual arms allows for the control of the resonance wavelength. The near-field distribution and local photocurrent patterns of the plasmonic nanostructures in the 4-7 port device and the 1.55-7 port device were investigated, as shown in Supplementary Fig. 9.

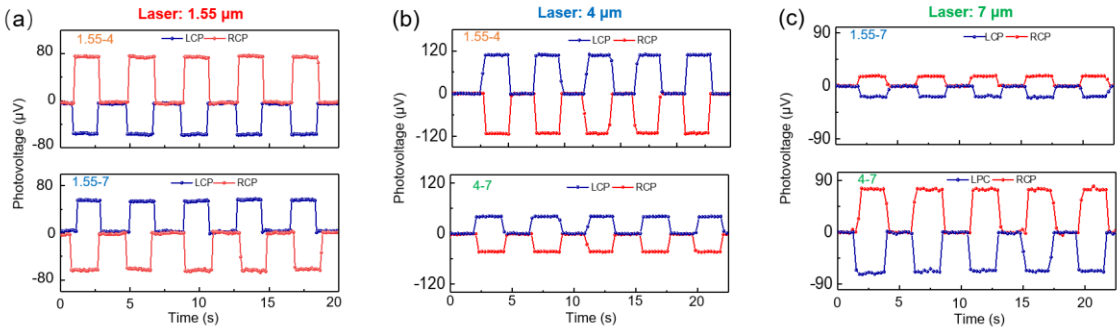

Supplementary Fig. 10. (a)-(c) The near-field distribution and local photocurrent patterns of the plasmonic nanostructures in the 4-7 port device and the 1.55-7 port device.

For each port, the LCP and RCP of the same design wavelength result in photocurrents with equal amplitude and opposite polarity. Additionally, the photovoltage amplitudes vary for different wavelengths of light. This makes it easy to distinguish light with different wavelengths and circular polarization information.

We explored the design of structures that operate in the visible/ultraviolet spectrum. Ultimately, with aluminum as the plasmonic material and dimensions as shown in Supplementary Fig. 11, we achieved a device capable of responding to circularly polarized light at a wavelength of 400 nm. Therefore, the operational wavelength range of this device is indeed designable.

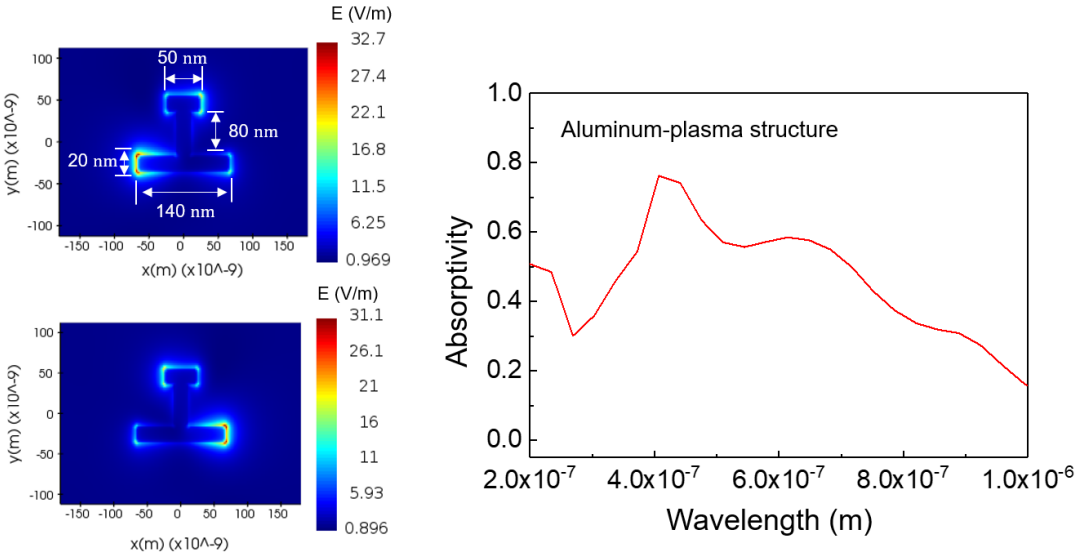

Supplementary Fig. 11 Design of a dual-arm plasmonic structure for the ultraviolet/visible light spectrum

Supplementary Note 3

3. Circular photogalvanic effect

A proficient circular polarization detector should exclusively respond to circularly polarized light while remaining impervious to the influence of linearly polarized components. Through the optimization of device dimensions, we ensure that the dual-arm plasmonic nanostructure maintains near-field mirror symmetry for linearly polarized light throughout, as illustrated in Figures S11a-d. This optimization is aimed at achieving global integration of the vector photocurrent equal to zero. However, in practical device fabrication processes, asymmetrical factors introduced by size discrepancies, doping, and other factors result in the device still exhibiting a response to linearly polarized light. To analyze this phenomenon, a circular photocurrent can be employed[10]:

$$I_{\mathrm{pc}} = C\sin(2\alpha + \varphi_{\mathrm{c}}) + \mathrm{L}\sin(4\alpha + \varphi_{\mathrm{l}}) + \mathrm{D} \tag{S15}$$

Here, α is the rotation angle of the quarter-waveplate, and φ_{c} and C are the circular photogalvanic effect (CPGE) current parameters, which characterize the valley polarity of the injected carriers. Another periodic term (manifested by φ_{l} and L) and a polarization-independent term D arise from the linear photogalvanic effect and its coupling to the CPGE. Figure S12e-f represent the extracted linearly polarized photocurrents and circularly polarized photocurrents, respectively, under light irradiation at wavelengths of 1.55 μm and 4 μm. The linearly polarized component is significantly smaller than the circularly polarized component, falling within an acceptable range.

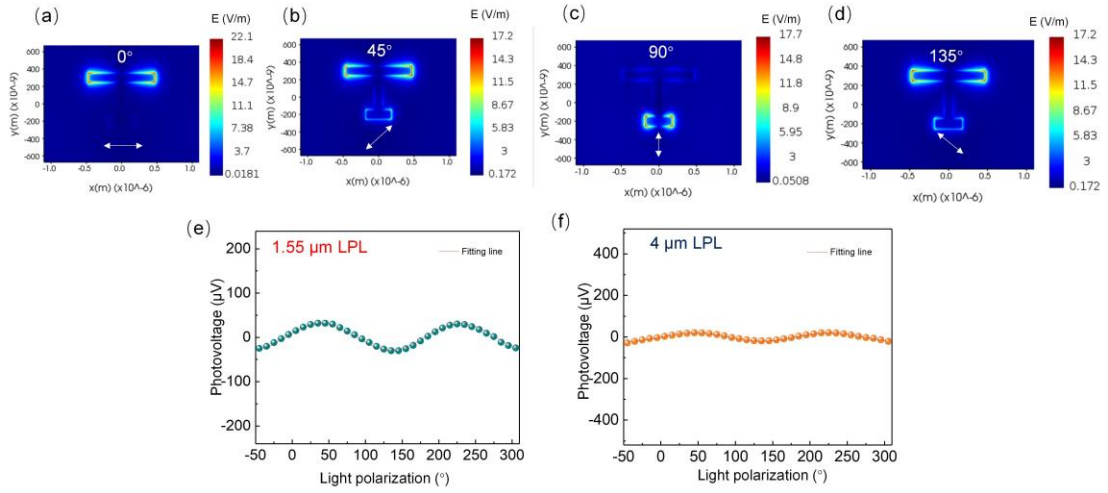

Supplementary Fig. 12. (a)-(d) The simulated near-field distribution of the dual-arm plasmonic nanostructure under various linearly polarized light conditions. **(e)-(f)** The extracted linear polarization component of the photocurrent under irradiation at wavelengths of 1.55 μm and 4 μm.

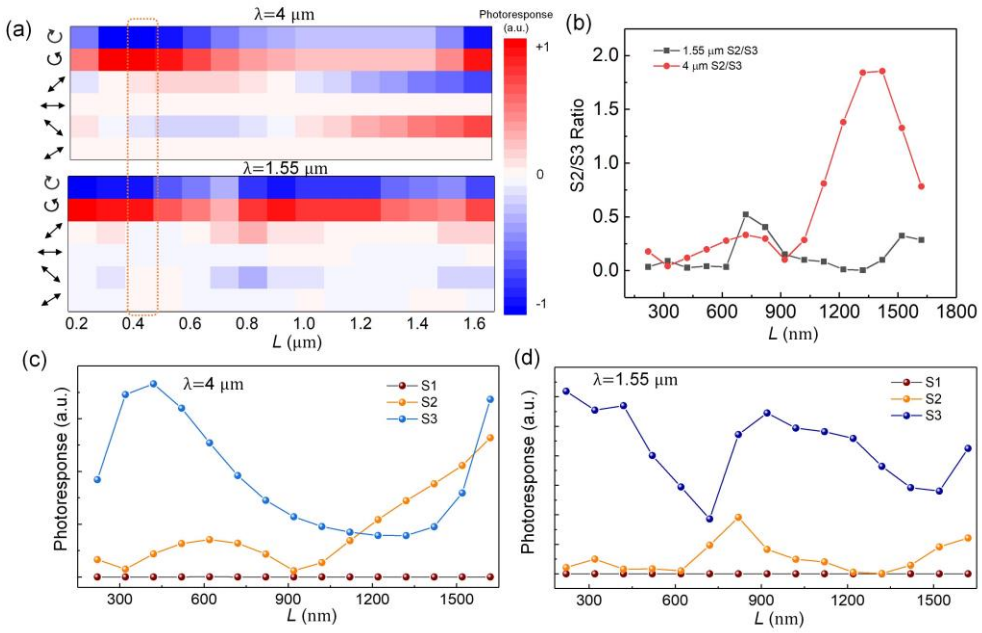

Supplementary Fig. 13. (a) The simulated photoresponse of device with different size to light with different polarization states. **(b)** The relationship between the ratio of parameters S2 to S3 and the device dimension *L*. **(c)-(d)** The variation of S-parameters with device dimension *L* across different wavelengths of 1.55 μm and 4 μm.

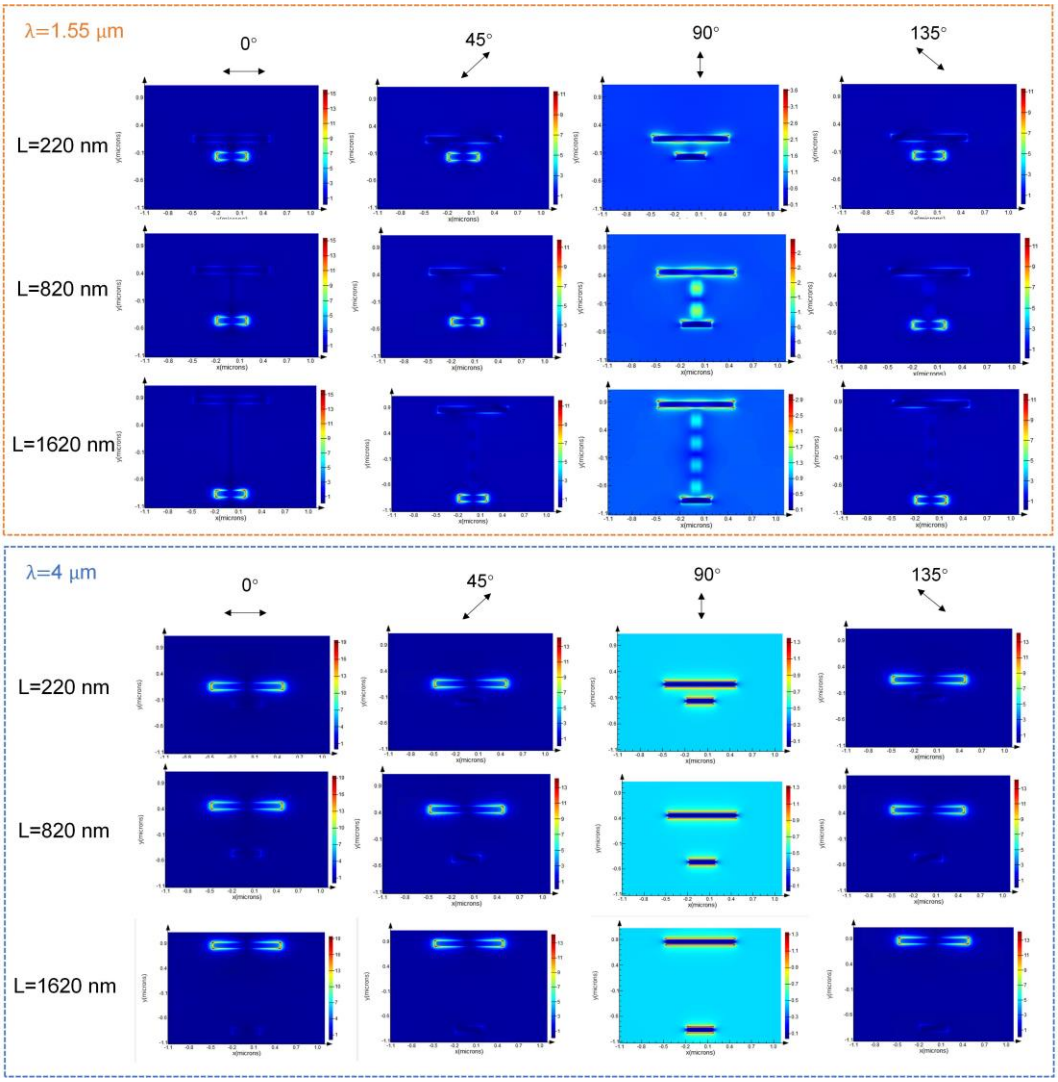

Supplementary Fig. 14. The near-field distribution of different wavelength linearly polarized light for devices of different sizes.

Supplementary Note 4

4. Photocurrent scanning test of the device.

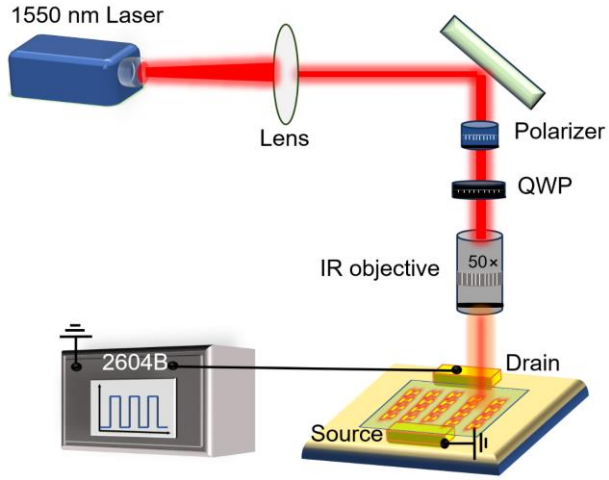

Supplementary Fig. 15. The setup for the photocurrent scanning test at 1.55 μm.

The testing platform consists of an optical setup, an electrical platform, and a displacement stage. For the optical setup, the entire optical path is built based on a cage structure. The 1550 nm laser is directed by a single-mode fiber to the homemade setup. The light passes through a lens, a polarizer, and a quarter-wave plate. The laser beam is focused by an objective into a sub micrometer diameter on the sample surface. For the electrical measurement setup, the current signal is read by the source meter 2604B and can be measured under either zero bias or biased conditions.

Local photocurrent scanning analysis

To gain a clearer understanding of the mechanisms and patterns of photocurrent generation, we conducted a 1.55 μm photocurrent mapping test on the device. A schematic diagram of the testing setup is shown in Supplementary Fig. 16a. The light beam emitted from the laser is focused through a lens and directed onto the vertical optical path by a mirror. It then passes through a polarizer and a quarter-wave plate, ultimately being transformed into a beam with a diameter of approximately 2 μm by a 50× objective before illuminating the sample. The scanned photocurrent signals were measured by a source meter (2604B). Microscopic and SEM images of the device are shown in Supplementary Fig. 16b. The blue dashed line box represents the scanning area, and the three spots A, B, and C correspond to locations inside the channel near the drain point, the middle point, and the source point, respectively.

The noncentrosymmetric shape of the nanoantennas can create large asymmetry in the local field via the plasmon localization effect. For the plasmonic double-armed nanostructure overlaying a graphene thin film, 1.55 μm circularly polarized light induces chiral near-field distributions localized on either side of the short arms, as shown in Supplementary Fig. 16c. LCP is localized on the left side, while RCP is localized on the right side. The resulting potential gradient leads to the generation of vectorial photocurrents in opposite directions, giving rise to bipolar photocurrents. Therefore, photocurrent scanning mapping can assist in obtaining localized photocurrent information.

Supplementary Fig. 16d-f shows the measured photocurrent during on-off cycles of LCP and RCP light illumination at points A, B and C. A zero external bias was applied ($V_d = V_g = 0$ V) here. The device exhibits photocurrents of opposite polarities when both LCP and RCP light are applied. The formation of photocurrents is a result of the accumulation of local vectorial photocurrents. Therefore, when the light spot is near the drain (point A), the local photocurrent generated by RCP light is more likely to migrate toward the drain, resulting in a greater magnitude of positive photocurrent. Conversely, when the light spot is near the source (point C), the local photocurrent generated by LCP light is more likely to migrate toward the source, resulting in a larger

magnitude of negative photocurrent. At the central position (point B), equal magnitudes of positive and negative photocurrents can be measured for both LCP and RCP light. Scanning images of the photocurrent map (Supplementary Fig. 16g and h) provide a clearer representation of the distribution characteristics of the photocurrent. Under RCP light illumination, the double-armed structure array within the channel accumulates vectorial photocurrents toward the drain side, resulting in an overall positive photocurrent distribution. In contrast, under LCP light illumination, vectorial photocurrents accumulate toward the source side, leading to an overall negative photocurrent distribution.

The above characterization data from the 1.55 μm local photocurrent scanning map show that this structure has a strong resolution ability for circularly polarized light, and compared to circular dichroism, the discrimination of bipolarity is more pronounced. For the double-armed nanostructure, in addition to the short arm used for the 1.55 μm resonance, the long arm exhibits opposite near-field localization characteristics at 4 μm. Hence, it effectively incorporates the wavelength dimension into the circular polarization detection dimension.

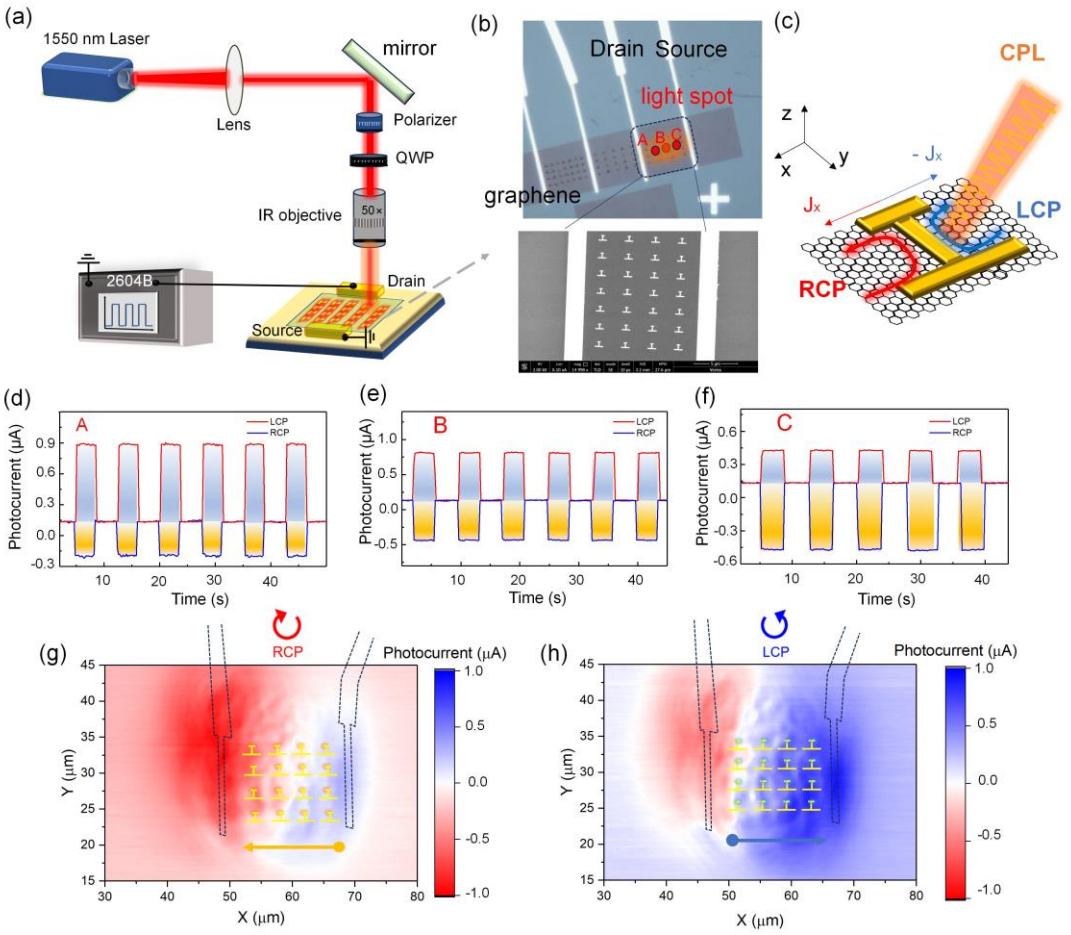

Supplementary Fig. 16. Photocurrent mapping, scanning and analysis. (a) Schematic diagram of the 1.55 μm photocurrent mapping scanning setup for the device. The light beam emitted from the 1.55 μm laser passes through a lens, polarizer, and quarter-wave plate and is further focused onto the sample using a 50× objective. **(b)** Microscopic and SEM images of the device. Points A, B, and C represent the positions where the light spots are irradiated onto the graphene channel. **(c)** Near-field analysis of plasmonic nanostructures for 1.55 μm circularly polarized light. Jx denotes the vectorial photocurrent along the x direction. For left-circular polarization (LCP) and right-circular polarization (RCP) light, the near fields are localized on the two sides of the short arm, thereby generating vectorial photocurrents in opposite directions along the x-axis. **(d)-(f)** The photocurrent switching signals obtained when 1.55 μm lasers in the LCP and RCP columns are, respectively irradiated at points A, B, and C. **(g)**, **(h)** Scanning images of photocurrent mapping measured by the device under LCP and RCP irradiation at 1.55 μm.

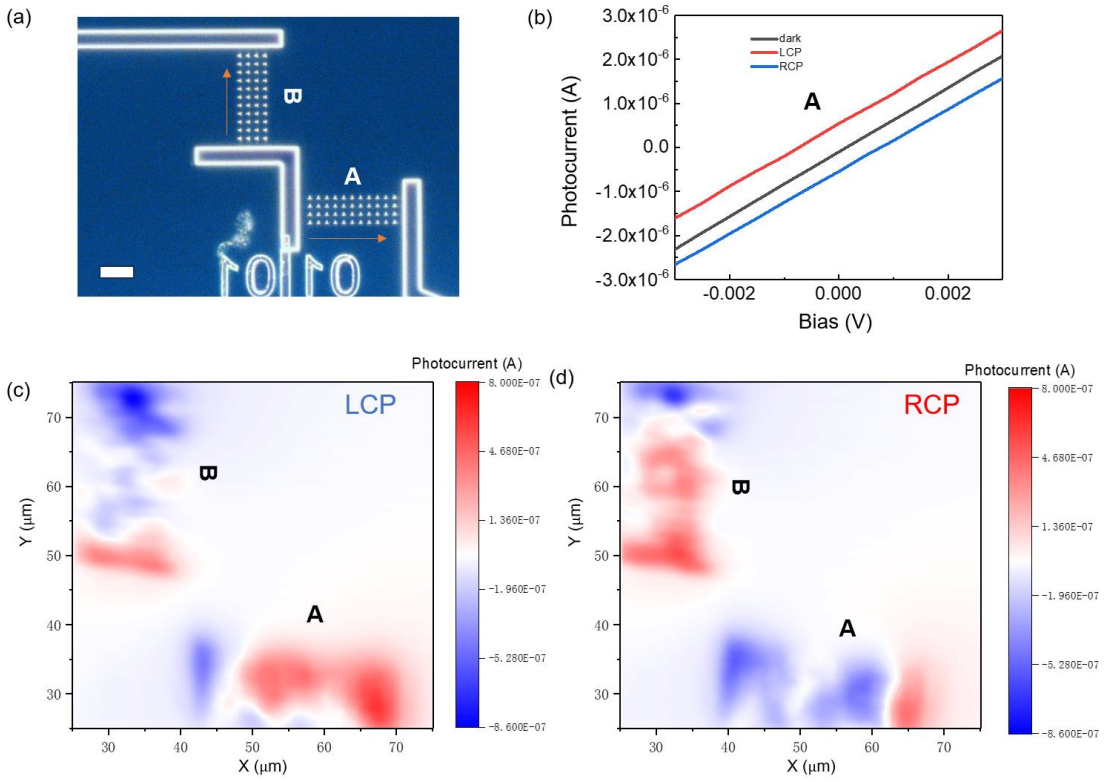

Supplementary Fig. 17. Photocurrent scanning test of the device under 1.55 μm. (a) dark-field microscope image of the vertical structure of the device. (b) I-V characteristic curves of devices in region A under different circularly polarized light. (c)-(d) Photocurrent scanning maps under different circularly polarized light conditions.

To validate the photocurrent generation patterns, we tested vertical structure devices using the constructed photocurrent scanning mapping apparatus. The vertically structured device is composed of interconnected dual-arm structures arranged in arrays A and B, which are oriented perpendicular to each other, as illustrated in Supplementary Fig. 17(a). When central region A was illuminated with LCP and RCP light, the corresponding I-V curves were measured, as shown in Supplementary Fig. 17(b). LPC and RCP resulted in positive and negative photocurrents, respectively. Further scanning of the entire device area with LCP and RCP light yielded photocurrent distribution maps, as shown in Supplementary Fig. 17(c) and (d), respectively. Both regions A and B, characterized by opposite orientations of the dual-arm nanostructure arrays, exhibit photocurrent distributions with opposite polarities.

Supplementary Note 5

5. Characterization of device performance

5.1 Responsivity and noise

The responsivity of devices can be obtained by:

$$R = \frac{\Delta I}{P_e} = (I_{light} - I_{dark}) \times (P \times \frac{S_{device}}{S_{light}})^{-1} \quad (S16)$$

where ΔI is the photocurrent, P is the optical power, and S_{device} and S_{light} are the areas of the active region and spot, respectively. Here, the optical power density can be defined as $\frac{P}{S_{light}}$. Because the spot area is significantly larger than the active area of the device and the central region of the spot in which the device is located is far from the region of power decay at the edges, it can be approximated as a uniform distribution of optical power. Therefore, the definition of optical power density is more applicable here.

Supplementary Table 1 Parameters for the responsivity characterization

Wavelength (μm)	Spot area (mm^2)	Power (mW)	Optical power density (mW/cm^2)	Device area (mm^2)
1.55	2.5	10	40	0.0006
4	10	40	40	0.0006
7	10	40	40	0.0006

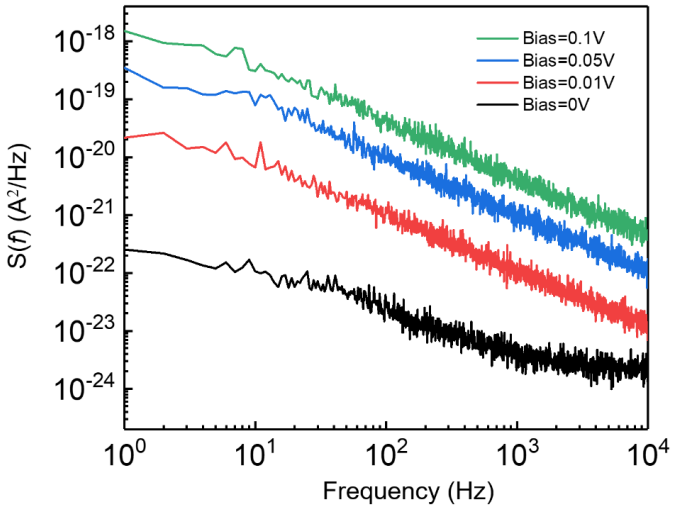

Supplementary Fig. 18. Current noise power spectral density of the device under different bias voltages.

The equivalent noise power (*NEP*) of the device was obtained by:[11]

$$NEP = \frac{\mathrm{i_n}}{R_p} = \frac{\sqrt{S(f_n)}}{R_p} \tag{S17}$$

where i_n is the noise current, $S(f_n)$ is the real-time measured current noise power spectral density, and f_n~ 1 kHz is the center frequency of the device. One advantage of zero-bias devices is that they exhibit extremely low current noise power spectral density compared to biased devices, particularly in the context of graphene-based devices. The detectivity can be obtained by:

$$D^* = \frac{\sqrt{A \cdot \Delta f}}{NEP} \tag{S18}$$

where A is the device area. For all three-port devices, the calculated responsivity, equivalent noise power, and ratio detection rate are presented in the following table.

Supplementary Table 2 Calculations of the responsivity, equivalent noise power (NEP), and ratio detection rate (D*) of the three-port device.

Device	Responsivity of CPL (mA/W)		
	1.55 μm	4 μm	7 μm
1.55-4	42	63	0
1.55-7	36.8	0.2	10.5
4-7	0.5	26.25	59
	NEP (pW/Hz $^{1/2}$)		
	1.55 μm	4 μm	7 μm
1.55-4	4.76	3.17	
1.55-7	5.43		1.90
4-7		7.62	3.39
	D* (Jones)		
	1.55 μm CPL	4 μm CPL	7 μm CPL
1.55-4	6.3×10^6	9.45×10^6	
1.55-7	5.52×10^6		1.58×10^6
4-7		3.94×10^6	8.85×10^6

5.2 Response time

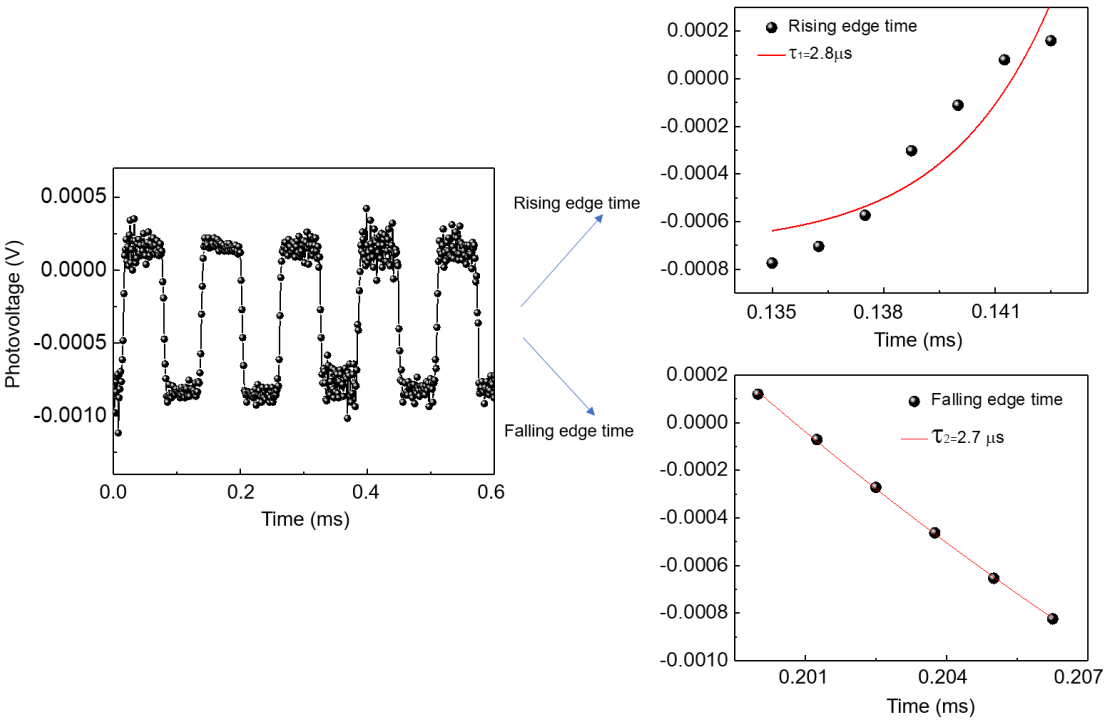

Supplementary Fig. 19. The optoelectronic switch signals of the device were collected by an oscilloscope, allowing for the measurement of both the rising and falling edge times.

5.3 Device stability testing

All tests in this study were conducted at room temperature and exhibited consistent performance over different time periods. To investigate the stability conditions and protection methods of the devices, we prepared devices both with and without hBN (hexagonal boron nitride) coverage and measured the performance stability (chopped signal) of both types of devices after long-term room temperature exposure. The performance of bare graphene devices deteriorated significantly due to adsorption effects from water vapor and other factors. However, the devices covered with hBN did not show substantial performance degradation. Additionally, the plasmonic structure is made of gold material, which is resistant to oxidation. Therefore, covering the material with hBN effectively maintains the stability of the device.

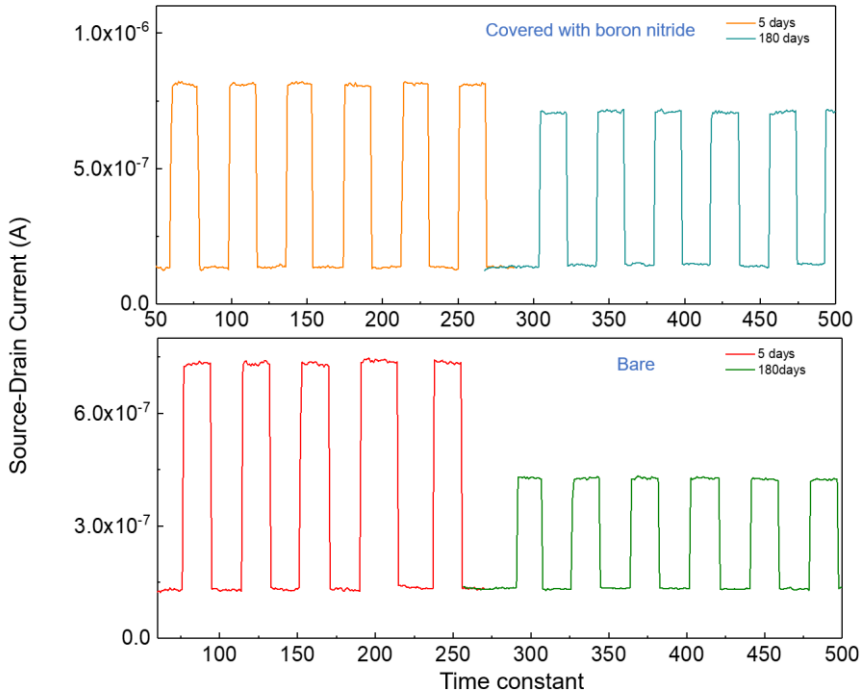

Supplementary Fig. 20. The performance stability (chopped signal) of devices with and without hBN after long-term room temperature exposure.

5.4 The linearity of photovoltage with illumination intensity

To explore the linearity of the photovoltage response to illumination intensity in the devices, we characterized them using a near-infrared test system with a spot size smaller than the area of the devices as shown in Supplementary Fig. 21. The measured power dependence of the polarization sensitivity indicates the extensive linear dynamic range of our device.

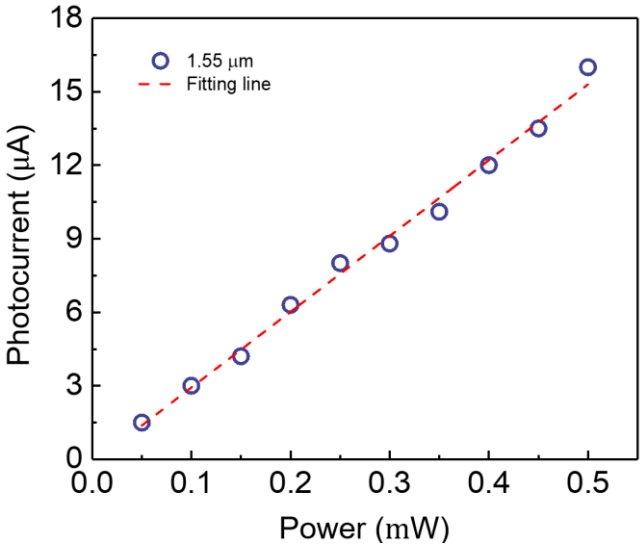

Supplementary Fig. 21. Measured correlation between responsivity and incident power dynamic range.

5.5 Comparison with typical infrared detectors

To evaluate the feasibility of our device for practical applications, we compared its performance with commercial detectors, as shown in Supplementary Table 3.

Supplementary Table 3. Comparison with typical infrared detectors

No	Description	Wavelength (μm)	Responsivity (V/W)	Bias Voltage	Ref. (with hyperlink)
1	Germanium photodiode	1.5	10	0-2 V	Nat. Photon. 15, 925 (2021)
2	InAsSb photovoltaic detector	4-5.9	21	0 V	P11120-201, Hamamatsu
3	Thermopile detector	0.19-20	0.1	0 V	TD10X, Thorlabs
4	Thermopile detector	3-5	50	0 V	T11361-01, Hamamatsu
5	This work	1.55-8	63	0 V	

5.6 Methods for optimizing device responsivity

We have investigated how to improve device responsivity. There are two main approaches:

1. By applying gate voltage to regulate the Schottky junction formed between graphene and the metal structure, the responsivity of the device can be modulated, as shown in Supplementary Fig. 22. Compared to devices without gate voltage, the photoresponse can increase by approximately five times when a gate voltage of 150V is applied. This demonstrates that gate voltage regulation is an effective method for enhancing device responsivity.

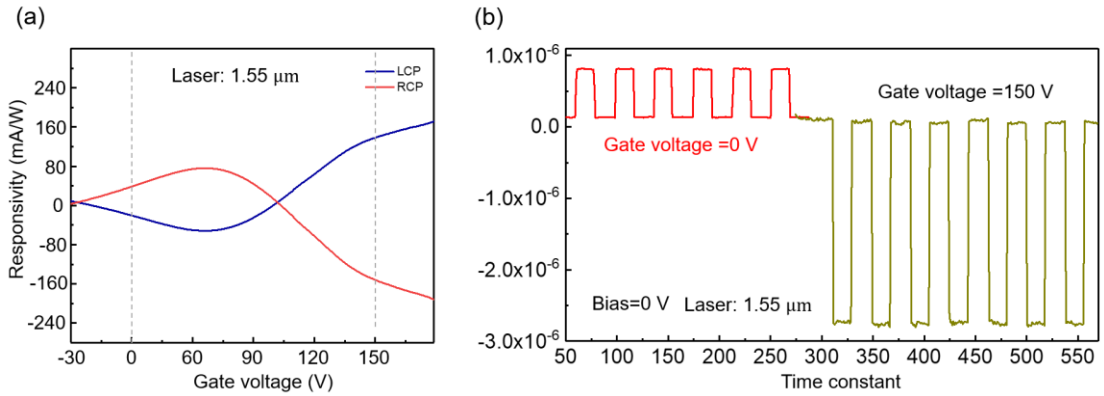

Supplementary Fig. 22. Performance comparison between three port devices and cascaded devices

2. We can play with the geometry of the graphene layer to increase the photoresponse. The device can be further miniaturized, as illustrated in Supplementary Fig. 23. Due to the increased length in the direction of the vector photocurrent, even with a channel width of only 10 μm, the signal strength increases fivefold. This indicates that device performance can be altered according to different requirements without sacrificing spatial resolution.

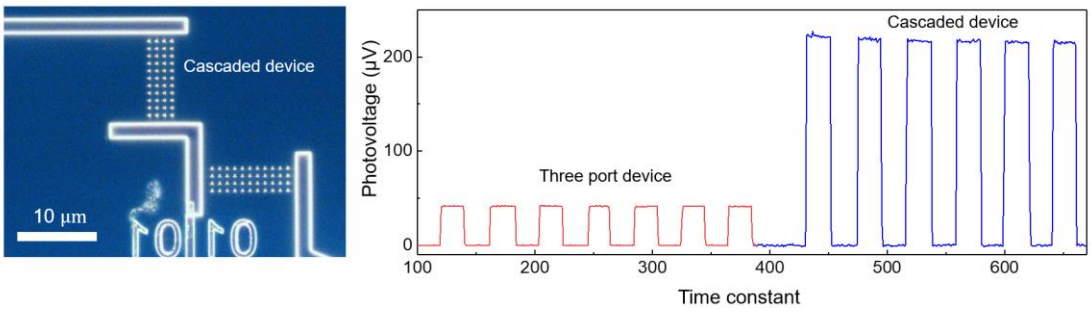

Supplementary Fig. 23. Performance comparison between three port devices and cascaded devices

In the process of exploring the aforementioned methods, the responsivity can be increased by approximately five times, and the corresponding detectivity can be enhanced to the order of 10^7.

5.6 Potential applications

Multiple degrees of freedom (such as wavelength, polarization, pulse length, etc.) that can be utilized for information encoding. However, achieving the next generation of high-capacity photonics requires sufficient channel capacity. This is why researchers are exploring orbital angular momentum detection, despite the significant challenges involved. Here, the dual optical incidence mode can lead to the superposition or cancellation of output signals, which can be utilized for the implementation of photonic logic gates. Today, the limitations of existing electronic logic gates in terms of precision and rapid computation, combined with the explosive demand for various data processing, have sparked interest in new logic gate platforms. The devices proposed in this paper can convert optical inputs into electrical outputs and perform multiple Boolean logics to realize photoelectric logic gate, as shown in Supplementary Fig. 24.

Dual light incidence mode

Input				Output
1.55 μm		4 μm		Signal
σ+	σ−	σ+	σ−	
1	1	0	0	NOT
1	0	1	0	NOR
1	0	0	1	AND
0	1	1	0	NAND
0	1	0	1	OR
0	0	1	1	NOT

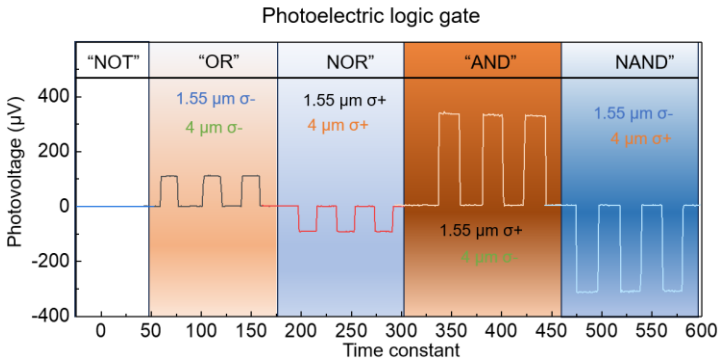

Supplementary Fig. 24. Demonstration of the photoelectric logic gate

Supplementary Note 6

6. Machine learning models

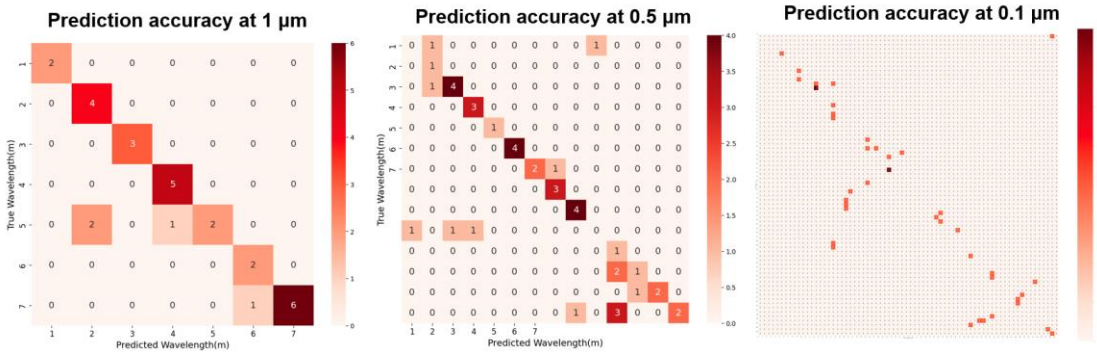

Supplementary Fig. 25. Confusion matrix for different prediction accuracies

Supplementary Table 4: Accuracy of Spin and Wavelength Prediction Model

Training accuracy		Test accuracy	
Spin Training	Wavelength Training	Spin Test	Wavelength Test
0.9375	0.9487	0.9285	0.8661

Note：The data in the table is reserved for four decimals

In the actual experiment of wavelength prediction, we constructed neural network models of varying complexity for wavelength prediction accuracy at 1 μm, 0.5 μm, and 0.1 μm. Due to the relatively small size of our database, when the wavelength prediction accuracy is at 0.1 μm, the model exhibits significant overfitting. These parts of the experimental results can be referred to in the Supplementary Fig. 25. However, it is worth noting that although the wavelength prediction accuracy discussed in the main text is at 0.5 μm, the method we have developed based on machine learning mechanisms for predicting spin and wavelength can achieve more accurate results when there is sufficient data in the database.

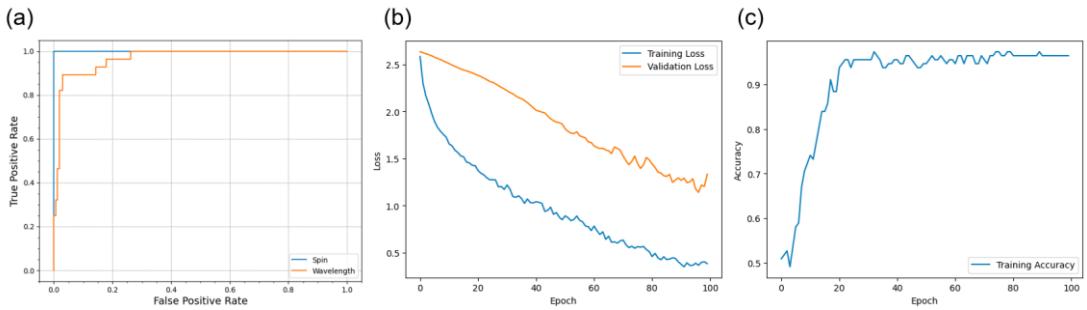

Supplementary Fig. 26. (a) The Receiver Operating Characteristic (ROC) curve, false positive rate is calculated as the proportion of negative samples that are incorrectly classified as positive， while the true positive rate is calculated as the proportion of positive samples that are correctly classified as positive. (b) The lose curve of training process, epoch is the number of models be trained fully using the samples in training set. (c) The various of accuracy as the epoch increase while the training process.

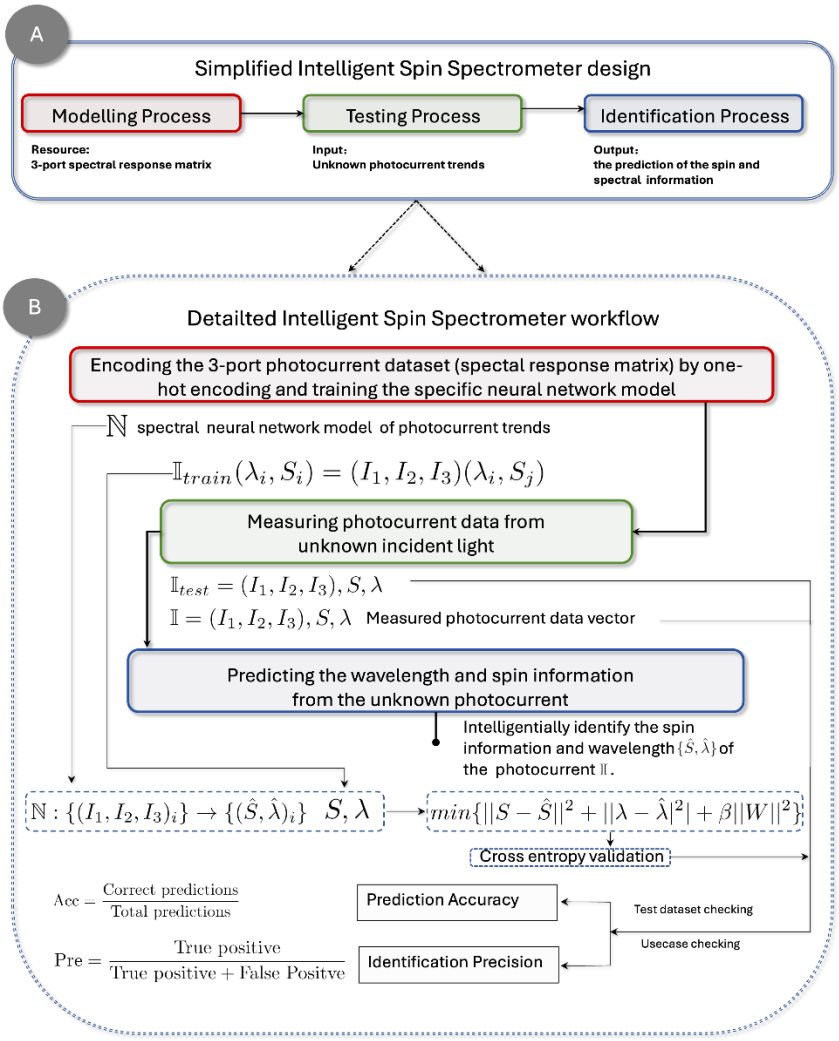

Supplementary Fig. 27. Summarized workflow diagram. A, Simplified version. B, Detailed version.

Supplementary Table 5. Comparison between this demonstration and other compact spectrometers

Method of spectral reconstruction	Footprint	Resolution /range	Spectral detection range	Spectral information	Ref.
Black phosphorus spectrometer	16 × 9 μm^2	1.19 %	2-9 μm	Wavelength	Nat. Photonics 15, 601–607 (2021)
Single-dot perovskite spectrometer	440 × 440 μm^2	1.28 %	350-750 nm	Wavelength	Adv. Mater. 34, e2200221 (2022)
ReS_2/Au/WSe_2 vdW spectrometer	6 × 4 μm^2	6.25 %	1150-1470 nm	Wavelength	Nat. Commun. 13, 4627 (2022).
MoS_2/WSe_2 vdW heterojunction	22 × 8 μm^2	0.68 %	405-845 nm	Wavelength	*Science.* **378**,296-299(2022)
This work	Radius~20 μm	1.42%	1-8 μm	Wavelength polarization	

Supplementary References

1. H. A. Haus, *Waves and fields in optoelectronics* (Prentice-Hall, New Jersey, 1984; https://books.google.com.sg/books/about/Waves_and_fields_in_optoelectronics.html?id=AQUpAQAAMAAJ&redir_esc=y).
2. S. Yi, M. Zhou, Z. Yu, P. Fan, N. Behdad, D. Lin, K. X. Wang, S. Fan, M. Brongersma, Subwavelength angle-sensing photodetectors inspired by directional hearing in small animals. *Nat. Nanotechnol.* **13**, 1143–1147 (2018).
3. S. Zu, T. Han, M. Jiang, F. Lin, X. Zhu, Z. Fang, Deep-Subwavelength Resolving and Manipulating of Hidden Chirality in Achiral Nanostructures. *ACS Nano*. **12**, 3908–3916 (2018).
4. A. Horrer, Y. Zhang, D. Gérard, J. Béal, M. Kociak, J. Plain, R. Bachelot, Local Optical Chirality Induced by Near-Field Mode Interference in Achiral Plasmonic Metamolecules. *Nano Lett.* **20**, 509–516 (2020).
5. G. Giovannetti, P. A. Khomyakov, G. Brocks, V. M. Karpan, J. van den Brink, P. J. Kelly, Doping Graphene with Metal Contacts. *Phys. Rev. Lett.* **101**, 026803 (2008).
6. T. Mueller, F. Xia, M. Freitag, J. Tsang, P. Avouris, Role of contacts in graphene transistors: A scanning photocurrent study. *Phys. Rev. B*. **79**, 245430 (2009).
7. Y. M. Zuev, W. Chang, P. Kim, Thermoelectric and Magnetothermoelectric Transport Measurements of Graphene. *Phys. Rev. Lett.* **102**, 096807 (2009).
8. Bandurin, D.A. et al. Negative local resistance caused by viscous electron backflow in graphene. *Science* **351**, 1055-1058 (2016).
9. Bandurin, D.A. et al. Fluidity onset in graphene. *Nature communications* **9**, 4533 (2018).
10. Yuan, H. et al. Generation and electric control of spin-valley-coupled circular photogalvanic current in WSe_2. *Nature nanotechnology* **9**, 851-857 (2014).
11. Fang, Y.J., Armin, A., Meredith, P. & Huang, J.S. Accurate characterization of next-generation thin-film photodetectors. *Nature Photonics* **13**, 1-4 (2019).